crystals

MDPI

Article

Insights into the Spray Synthesis of UiO-66 and UiO-66-NH_2 Metal–Organic Frameworks: Effect of Zirconium Precursors and Process Parameters

Masaru Kubo *, Yusuke Miyoshi, Yushi Uchitomi and Manabu Shimada

Department of Advanced Science and Engineering, Graduate School of Advanced Science and Engineering, Hiroshima University, Kagamiyama 1-4-1, Higashi-Hiroshima 739-8527, Hiroshima, Japan; smd@hiroshima-u.ac.jp (M.S.)

* Correspondence: mkubo@hiroshima-u.ac.jp; Tel.: +81-82-424-7851

Abstract: UiO-66, a zirconium-based metal–organic framework, was synthesized using a one-step spray synthesis method to investigate the effects of preheating the precursor solution and Zr sources on crystallinity. Using $ZrCl_4$ with water as a modulator requires preheating at 80 °C for 120 min or 120 °C for 30 min for the spray synthesis of UiO-66 to form secondary building units (SBUs). By contrast, the use of Zr(O*n*Pr)$_4$ with acetic acid (AcOH) as a modulator allowed the spray synthesis of UiO-66 and UiO-66-NH_2 without preheating because of the rapid formation of SBUs with AcOH. The spray-synthesized UiO-66 using Zr(O*n*Pr)$_4$ exhibited a BET surface area of 1258 m^2/g and a CO_2 adsorption capacity of 3.43 mmol/g at 273 K and 1 bar, while UiO-66-NH_2 exhibited a BET surface area of 1263 m^2/g and a CO_2 adsorption capacity of 6.11 mmol/g under the same conditions.

Keywords: secondary building units; preheating; CO_2 adsorption

check for updates

Citation: Kubo, M.; Miyoshi, Y.; Uchitomi, Y.; Shimada, M. Insights into the Spray Synthesis of UiO-66 and UiO-66-NH_2 Metal–Organic Frameworks: Effect of Zirconium Precursors and Process Parameters. *Crystals* **2024**, *14*, 116. https://doi.org/10.3390/cryst14020116

Academic Editor: Ferdinando Costantino

Received: 27 December 2023
Revised: 19 January 2024
Accepted: 23 January 2024
Published: 24 January 2024

Copyright: © 2024 by the authors. Licensee MDPI, Basel, Switzerland. This article is an open access article distributed under the terms and conditions of the Creative Commons Attribution (CC BY) license (https://creativecommons.org/licenses/by/4.0/).

1. Introduction

Metal–organic frameworks (MOFs) comprising metal ions or metal clusters as nodes and multitopic organic ligands as linkers represent an emerging class of porous crystalline materials with diverse applications, including gas storage and separation, catalysis, drug delivery, and sensing [1–5]. Zirconium MOFs (Zr-MOFs) are a subclass of MOFs comprising zirconium oxide clusters ($Zr_6O_4(OH)_4$) and secondary building units (SBUs) as nodes [6]. UiO-66 (UiO = University of Oslo), the first Zr-MOF that utilized 1,4-benzenedicarboxylate (BDC^{2-}) as a linker [7], is a promising candidate for industrialization and commercialization owing to its exceptional thermal, acidic, aqueous, and mechanical stabilities, which are attributed to its robust Zr–O bond [7,8].

To facilitate the commercialization of MOFs, including UiO-66, it is imperative to develop scalable, sustainable, and cost-effective production processes [9,10]. Solvothermal synthesis in a batch system, in which raw materials are dissolved in an organic solvent and then heated, is a common method for the lab-scale synthesis of MOF. However, scaling up a batch process presents challenges because of the dependence of heat and mass transfer on the reactor size. Continuous processes, such as flow reactors [11–13], countercurrent mixing reactors [14], continuous stirred-tank reactors (CSTR) [15], and spray synthesis [16–19], offer the advantages of maintaining consistent conditions and reducing time and energy costs.

Inspired by the well-known spray-drying technique, the spray synthesis process involves the crystallization of MOF particles in sprayed droplets of a precursor solution during solvent evaporation [16–19]. This technique has several advantages compared to solvothermal synthesis: continuous production in one step, high yields, low product moisture content, unnecessary separation of the product from the solvent, and reduced reaction time. Several MOFs have been successfully synthesized using this method by directly spraying a precursor solution [16,17]. However, the spray synthesis of UiO-66 assembled

from polynuclear SBUs remains challenging, because it requires the pre-formation of SBUs with an organic linker before assembly. The fast evaporation time of the spray synthesis is not sufficient to form SBUs and assemble them into UiO-66 using a precursor solution without any treatment. Hence, the spray synthesis of UiO-66 requires preheating the precursor solution before spraying as SBUs are formed during preheating [16]. Although the spray synthesis process reduces the number of steps required, preheating requires additional steps and energy consumption. Therefore, the spray synthesis of UiO-66 without preheating is desired.

This study aimed to investigate the effects of preheating on the spray synthesis of UiO-66 and propose a procedure for spray synthesis without preheating. Zirconium chloride ($ZrCl_4$) and zirconium propoxide ($Zr(O\mathit{n}Pr)_4$) served as Zr sources, with H_2O and acetic acid (AcOH) acting as modulators to control the crystal nucleation and growth rates of UiO-66 [20]. The obtained samples were analyzed by X-ray diffraction, which revealed that UiO-66 could be spray synthesized without preheating using $Zr(O\mathit{n}Pr)_4$ and AcOH. UiO-66-NH_2 was successfully spray synthesized using this method, and the CO_2 adsorption properties of the spray-synthesized UiO-66 and UiO-66-NH_2 were evaluated.

2. Materials and Methods

2.1. Chemicals

Zirconium(IV) chloride ($ZrCl_4$), zirconium(IV) propoxide ($Zr(O\mathit{n}Pr)_4$, ~70% in 1-Propanol), terephthalic acid (H_2BDC), and 2-aminoterephthalic acid (H_2BDC-NH_2) were purchased from TCI Chemicals (Tokyo, Japan). N, N-Dimethylformamide (DMF, 99%), acetic acid (AcOH, 99.7%), hydrochloric acid (HCl, 37% in H_2O), and nitric acid (HNO_3, 60–62%) were purchased from Fuji-film Wako Pure Chemical Co. (Osaka, Japan). All the reagents were used without further purification.

2.2. Precursor Solution of UiO-66 Using $ZrCl_4$ as a Zr Source

$ZrCl_4$ (0.35 g, 1.50 mmol) and H_2BDC (0.250 g, 1.50 mmol) were dissolved in DMF (13.5 g, 185.3 mmol) and deionized H_2O (0.812 g, 45.1 mmol) in a Teflon bottle. The mixture was heated at 80 °C for the precursor solution of spray synthesis and at 120 °C for batch synthesis. The batch-synthesized samples were collected by centrifugation, washed with fresh DMF, and then with ethanol. After ethanol washing, the samples collected by centrifugation were then dried at 80 °C for 6 h.

2.3. Precursor Solution of UiO-66 and UiO-66-NH_2 Using $Zr(OnPr)_4$ as a Zr Source

A 0.200 g of ca. 70% solution of $Zr(O\mathit{n}Pr)_4$ in *n*-propanol (0.140 g, 0.427 mmol) was added to a cosolvent of DMF (18.0 g, 246.3 mmol) and AcOH (3.60–11.36 g, 59.8–189.3 mmol). To confirm the effect of pH, HNO_3 was added to adjust the pH to 1.6 by replacement of AcOH (AcOH/Zr molar ratio of 440) in the Zr solution. The resulting Zr solution was stirred at 500 rpm for 20 min at room temperature. The organic linker solution was prepared by dissolving H_2BDC (0.071–0.178 g, 0.427–1.22 mmol) or H_2BDC-NH_2 (0.193–0.464 g, 1.07–2.56 mmol) in DMF (5.55 g, 76.0 mmol). The two solutions were mixed and immediately applied to a spray apparatus. For batch synthesis, mixtures with molar ratios of Zr: organic linker: AcOH: DMF of 1:2.5:440:756 for UiO-66, and 1:5:440:756 for UiO-66-NH_2 were stirred at 500 rpm for 24 h at room temperature.

2.4. Spray Synthesis of UiO-66 and UiO-66-NH_2

UiO-66 was synthesized using a homemade apparatus for spray synthesis [19,21,22]. The apparatus, as schematically depicted in Figure S1 in Supplementary Materials, comprised a two-fluid nozzle (MMA-10, Everloy, Hyogo, Japan), spray chamber, heating tube, and filter holder. The precursor solution, prepared as outlined below, was fed into the two-fluid nozzle via a syringe pump at a flow rate of 1 mL/min, and clean air was simultaneously sprayed at a flow rate of 12 L/min. The sprayed droplets were heated in a heating tube at 180 °C. The samples were collected using a glass filter. The collected samples were

washed via ultrasonication in DMF and ethanol to eliminate residual precursors. After washing by ethanol three times, the samples collected by centrifugation were then dried at 80 °C for 6 h.

2.5. Characterizations

Powder X-ray diffraction (XRD) patterns were measured using Miniflex 600 (Rigaku Corp., Tokyo, Japan) with Cu Kα radiation (wavelength: 1.5406 Å), an acceleration voltage at 40 kV, step size of 0.02°, and scan speed of 10°/min. Nitrogen adsorption–desorption measurements were conducted using an automated micropore gas analyzer (AUTOSORB-1-MP, Quantachrome Instruments, Boynton Beach, FL, USA) at 77 K after sample activation at 180 °C and 0.1 Pa for 6 h. The specific surface areas of the samples were calculated from nitrogen adsorption isotherms using the Brunauer–Emmett–Teller (BET) method in the range of $0.01 < P/P_0 < 0.05$. The micropore volumes were calculated using the *t*-plot method. The pore size distribution was determined using the Barrett–Joyner–Halenda (BJH) method. CO_2 adsorption measurements were conducted using AUTOSORB-1-MP with a thermostat (CryoSync, Quantachrome Instruments, FL, USA) at 273 K and 298 K after sample activation at 180 °C and 0.1 Pa for 6 h. The isosteric heat of adsorption (Q_{st}) was calculated using the Clausius–Clapeyron equation:

$$Q_{st} = R\left(\frac{\partial \ln P}{\partial 1/T}\right)_{w_a} \quad (1)$$

where R is the gas constant, P is the pressure, w_a is the CO_2 uptake, and T is the temperature. Thermogravimetric-differential thermal analyses (TG-DTA) were conducted in air up to 600 °C (10 °C/min) on a TG/DTA6200 (Hitachi High-Tech Corp., Tokyo, Japan).

3. Results

3.1. Spray Synthesis of UiO-66 Using $ZrCl_4$ as a Zr Source

Figure 1 shows the XRD patterns of the samples spray-synthesized UiO-66 at different preheating times and temperatures. The sample without preheating exhibited a broad peak at 8.2°, indicating that UiO-66 was not synthesized [20,23]. As the preheating time increases, the peak splits into two peaks at 7.3° and 8.5°, which are attributed to the (111) and (200) planes of the UiO-66 crystal structure, respectively. These peaks became sharper for preheating times of 60 min or longer, and additional peaks associated with other planes emerged, which aligned well with the simulated patterns. Higher preheating temperatures (120 °C) yielded UiO-66 in a shorter time of 30 min. However, without H_2O addition to the precursor solution, UiO-66 was not obtained even after preheating for 120 min at 80 °C (Figure S2). The effect of the temperature on droplet heating was also studied. Figure S3 shows the XRD patterns of the UiO-66 spray synthesized at different temperatures in the heating tube. The crystallinity of UiO-66 decreases with increasing temperature in the heating tubes.

To confirm that UiO-66 was crystallized in droplets, a solvothermal reaction in the batch process was conducted at 120 °C with different heating times. Figure 2 shows the XRD patterns of the samples, revealing that UiO-66 was obtained when the heating time exceeded 16 h. Within the initial 2 h heating time, the solution remained transparent, and the particles could not be collected by centrifugation. This suggests that UiO-66 crystallization occurred not during preheating, but through droplet evaporation. The samples obtained at heating times of 4 and 6 h exhibit a broad peak at 8.2 °C, indicating that UiO-66 was not crystallized during this period.

Figure 3 shows SEM images, nitrogen adsorption isotherms, and pore size distribution of the batch-synthesized UiO-66 and the spray-synthesized UiO-66 with preheating at 80 °C for 120 min before and after washing using $ZrCl_4$ as the Zr source. Hereafter, these three samples are referred to as b-UiO-66(Cl), unwashed-sp-UiO-66(Cl), and sp-UiO-66(Cl).

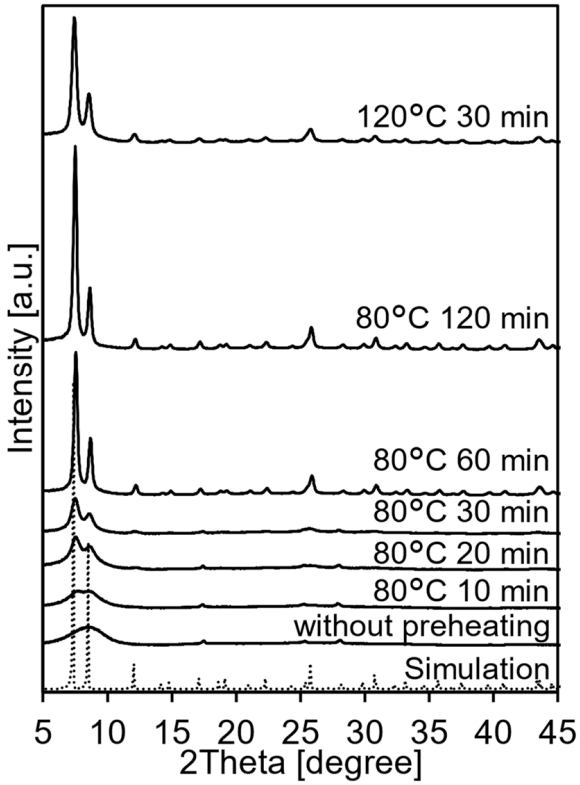

Figure 1. XRD patterns of spray-synthesized UiO-66 with different preheating times and temperatures using $ZrCl_4$ as the Zr source.

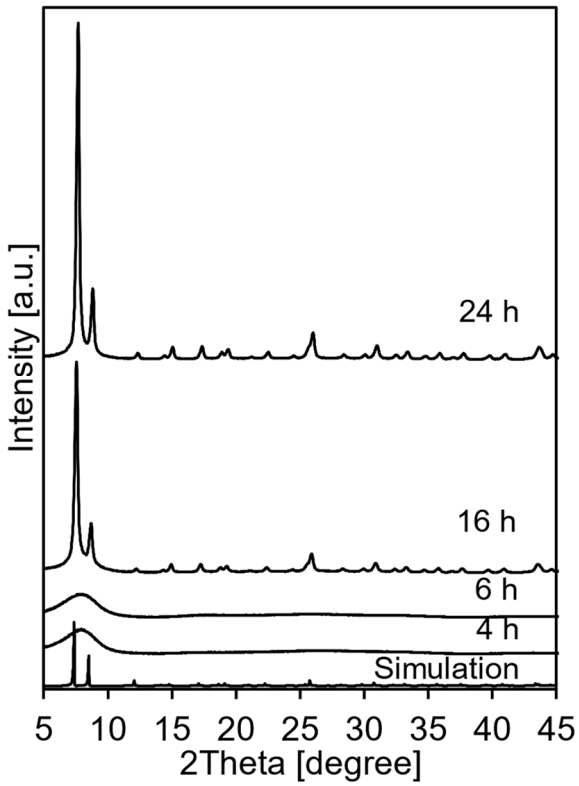

Figure 2. XRD patterns of the samples obtained by a solvothermal reaction using $ZrCl_4$ as the Zr source in a batch process with different heating times.

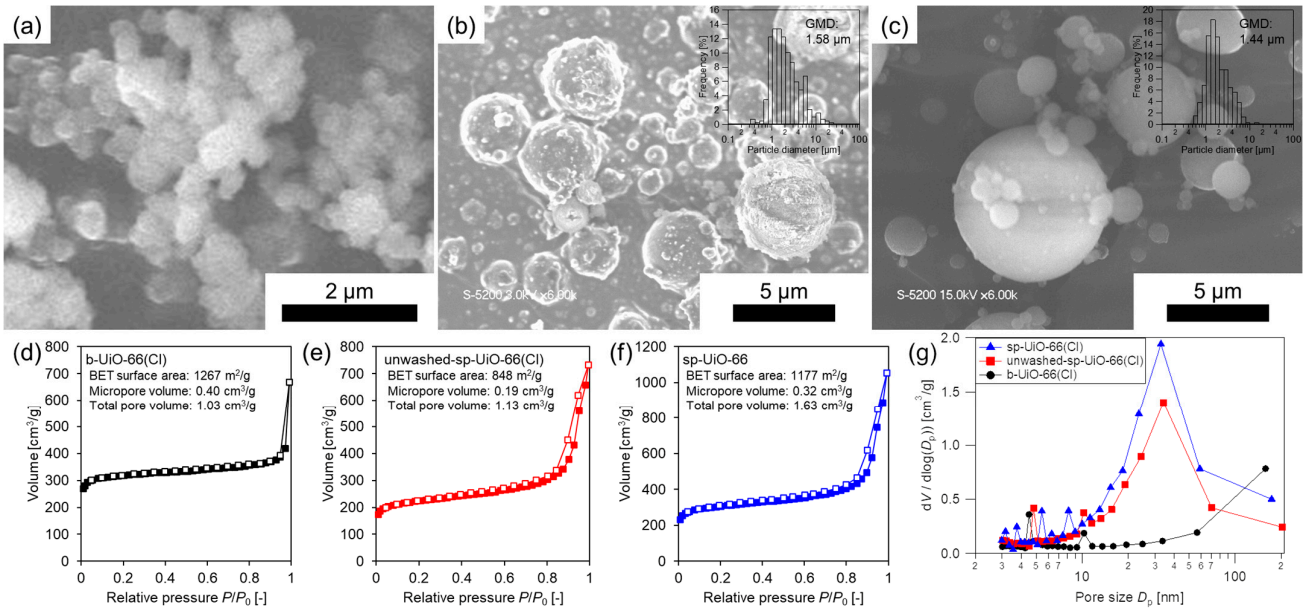

Figure 3. (**a**–**c**) SEM images, (**d**–**f**) nitrogen adsorption isotherms (filled: adsorption branch; opened: desorption branch), and (**g**) BJH pore size distribution of b-UiO-66(Cl), unwashed-sp-UiO-66(Cl), and sp-UiO-66(Cl); insets of (**b**,**c**) are particle size distributions.

The SEM image of b-UiO-66(Cl) (Figure 3a) shows nanoparticles with diameters of approximately 300 nm. In the spray synthesis method (Figure 3b,c), spherical particles were observed as unwashed-sp-UiO-66(Cl) and sp-UiO-66(Cl). A spherical morphology is common for particles prepared using the spray-drying method [24]. Notably, the spherical morphology was maintained after washing, indicating that washing did not cause particle collapse. The Feret diameter was estimated from the SEM images of the spray-synthesized UiO-66. There was no significant difference in the particle size distributions, with the geometric mean diameters (GMDs) of 1.97 μm for unwashed-sp-UiO-66(Cl) and 1.80 μm for sp-UiO-66(Cl).

The nitrogen adsorption isotherms of the three samples exhibited a combination of type I and IV isotherms, indicating that the samples contained both micro- and mesopores. The BET surface area and micropore volume of b-UiO-66(Cl) are 1267 m^2/g and 0.40 cm^3/g, respectively, consistent with previous results [7,25]; the results for the spray-synthesized UiO-66 are 848 m^2/g and 0.19 cm^3/g for unwashed-sp-UiO-66(Cl) and 1177 m^2/g and 0.32 cm^3/g for sp-UiO-66(Cl), respectively. The low surface area and micropore volume of the unwashed-sp-UiO-66(Cl) could be due to clogging of the micropores of the UiO-66 crystals by unreacted impurities, which can be removed by washing. The total pore volumes of unwashed-sp-UiO-66(Cl) and sp-UiO-66(Cl) are 1.13 and 1.63 cm^3/g, respectively, higher than that of b-UiO-66. The high total pore volume of sp-UiO-66(Cl) was due to the mesopores of approximately 30 nm, as shown in the pore size distributions (Figure 3g).

Yield of the spray synthesis was evaluated: yields and purities were 21.7 mg/mL and 92% for b-UiO-66(Cl), and 9.1 mg/mL and 71% for sp-UiO-66(Cl), respectively. The spray synthesis yield was lower because of the presence of impurities and losses due to deposition onto the tubes. Using these values, the ideal yields per unit time, considering the preheating time, were estimated, which increased with the volume of the precursor solution used, as shown in Figure S4. When 15 mL of the solution was used, in other words 15 min for spraying, the yield per times of sp-UiO-66(Cl) was 60.7 mg/h, which is 4.5 times higher than that for b-UiO-66(Cl) (13.5 mg/h). However, the yield per spray synthesis time was lower than that of batch synthesis above 450 mL of the solution. However, in batch synthesis, an increase in the solution volume slows the heat-transfer rate and causes

a decrease in the yield [26]. For spray synthesis, the yield per unit time was improved by decreasing the deposition loss and improving purity.

The crystallization mechanism of UiO-66 in droplets via spray synthesis using $ZrCl_4$ as the Zr source is illustrated in Scheme 1. The formation of SBUs is crucial for the synthesis of MOFs assembled from polynuclear SBUs, because they play key roles in nucleation and subsequent crystal growth [17]. $Zr_6O_4(OH)_4$ clusters (Zr clusters) with an octahedral structure, that is, the SBU of UiO-66, are formed in the presence of water [27,28]. In solvothermal reactions, Zr clusters are formed as SBUs in the initial heating stage and subsequently undergo ligand coordination with BDC^{2-} to grow UiO-66 crystals, as confirmed by in situ pair distribution function analysis [27].

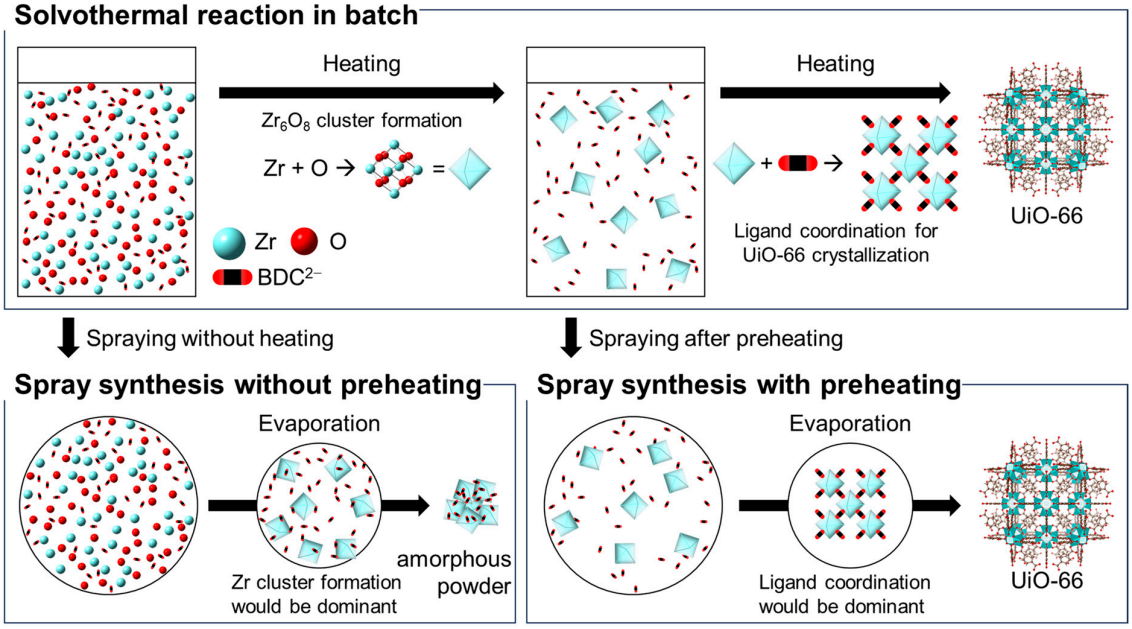

Scheme 1. Crystallization mechanism of UiO-66 under solvothermal reaction in batch and spray synthesis without and with preheating.

The Zr cluster concentration in the sprayed solution was low with no or short preheating. Consequently, the dominant product during droplet evaporation was Zr clusters or amorphous complexes rather than UiO-66 crystallization, as evidenced by the broad peak at 8.2° in the XRD patterns (Figure 1). However, UiO-66 was successfully synthesized with a sufficient preheating time. This indicated that Zr clusters formed during preheating and subsequently grew into UiO-66 crystals through ligand coordination with BDC^{2-} during droplet evaporation.

The crystallization of UiO-66 was also affected by the balance between the concentrations of Zr clusters and BDC^{2-} within a droplet, which was altered by the consumption due to crystal growth and concentration due to solvent evaporation. The evaporation time from a droplet with a diameter of 10 mm was calculated as 1.0 ms at 180 °C and 0.63 ms at 250 °C by Maxwell's method [29] (shown in Figure S5). Indeed, the crystallinity of UiO-66 decreased with increasing heating tube temperature, as shown in Figure S3. Rapid evaporation at higher temperatures results in insufficient crystal growth. Therefore, the crystallization of UiO-66 requires not only the formation of Zr clusters, but also a delicate balance between crystal growth and evaporation rate.

Other additives, such as acetic acid (AcOH) and hydrochloric acid (HCl), were used to confirm the formation of Zr clusters without preheating. AcOH is known as a modulator to slow the crystallization of UiO-66 [20]. In contrast, HCl, as a modulator, promotes crystallization [30]. Figure S6 shows XRD patterns of the spray synthesized samples without preheating and with additives. The sample with HCl exhibited the same broad

peak at 8.2° as that with H_2O. The addition of AcOH, as well as AcOH and HCl, resulted in a small shoulder peak at 7.3°, which was attributed to the (111) plane of UiO-66. This result suggests that a small number of Zr clusters were formed in the presence of AcOH. However, highly crystalline UiO-66 could not be obtained owing to its low Zr cluster concentration. We concluded that $ZrCl_4$ is not suitable for spray synthesis without preheating. In addition, when $ZrCl_4$ was used as the Zr source, HCl was inevitably produced as a by-product of UiO-66, which caused rusting of the apparatus. Therefore, we decided to use other precursors as Zr sources.

3.2. Spray Synthesis of UiO-66 Using Zr(OnPr)$_4$ as a Zr Source without Preheating

We chose Zr(O*n*Pr)$_4$ as an alternative Zr source because it is a non-corrosive precursor and is compatible with the synthesis of UiO-66 in the presence of AcOH, where the amount of AcOH influences the BET surface area of the synthesized UiO-66 [31]. DeStefano et al. demonstrated a room-temperature synthesis method for UiO-66, wherein SBUs were initially formed from Zr(O*n*Pr)$_4$ in the presence of AcOH at 130 °C, followed by a subsequent reaction of the preformed intermediate with a higher-than-stoichiometric concentration of the H_2BDC linker (H_2BDC/Zr = 2.85) [32]. With this information in hand, we conducted a batch synthesis of UiO-66 by preforming SBUs with varying AcOH/Zr ratios at room temperature by stirring for 20 min.

Figure 4a shows the XRD patterns of the batch-synthesized UiO-66 with Zr(O*n*Pr)$_4$ and different AcOH/Zr ratios. At an AcOH/Zr ratio of 140, a broad peak was observed at 8.2°, indicating insufficient formation of SBUs. As the AcOH/Zr ratio increased, the peaks split, and two distinct peaks were observed for the ratio of 340. Beyond a ratio of 440, the XRD patterns exhibited other peaks in addition to the (111) and (200) planes of UiO-66. Therefore, we decided to perform spray synthesis without preheating using a solution with an AcOH/Zr ratio above 140, where the peaks began to split.

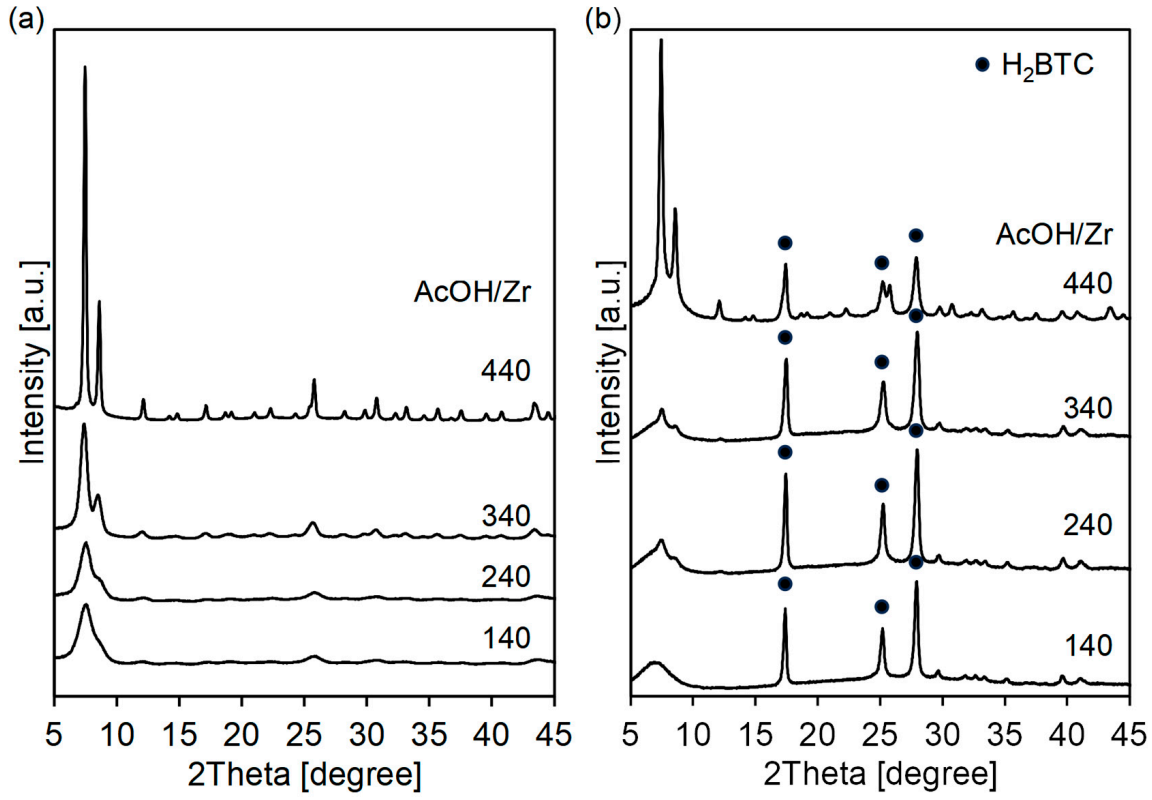

Figure 4. XRD patterns of (**a**) batch-synthesized UiO-66 at room temperature with Zr(O*n*Pr)$_4$ and different AcOH/Zr ratios and (**b**) spray-synthesized UiO-66 before washing with different AcOH/Zr ratios (H_2BDC/Zr = 2.5).

Figure 4b shows the XRD patterns of unwashed UiO-66, which was spray synthesized after preforming Zr clusters with varying AcOH/Zr ratios (140–440). UiO-66 was successfully synthesized for the first time at an AcOH/Zr ratio of 440 using spray synthesis without preheating. However, peaks attributed to H_2BDC were also observed because of excess H_2BDC in the droplet. These peaks disappeared after the washing. The crystallinity of the samples increased with the AcOH/Zr ratio. Slightly split peaks were observed at 7.3° and 8.5° when the AcOH/Zr ratios were 240 and 340, respectively, whereas a broad peak was observed at 8.2° when the AcOH/Zr ratio was 140.

The formation of Zr clusters was crucial for the crystallization of UiO-66. Zr(O*n*Pr)$_4$ forms an acetate cluster, $[Zr_6O_4(OH)_4(CH_3COO)_{12}]_2$, in the presence of AcOH [33,34]. The substitution of HNO_3 with AcOH at the same pH (1.6) produced low-crystallinity UiO-66 (Figure S7). This indicates that pH does not contribute to the formation of UiO-66 by spray synthesis, and that AcOH with a carboxyl group is essential for forming this cluster. The AcOH/Zr ratio was also critical for obtaining UiO-66 via spray synthesis. The reaction between Zr(O*n*Pr)$_4$ and AcOH for cluster formation was performed by stirring for 20 min at room temperature. Increasing the aging time to 24 h improves the crystallinity at lower AcOH/Zr ratios (Figure S8). Particularly, at the ratio of 340, the intensity of the peak at 7.3° is consistent with that of the sample aged for 20 min at a ratio of 440. This indicates that both the AcOH/Zr ratio and aging time are essential for the spray synthesis of UiO-66 using Zr(O*n*Pr)$_4$ without preheating.

Figure 5 shows the XRD patterns of the spray-synthesized UiO-66 after washing with different H_2BDC/Zr ratios. Precipitation occurred immediately after mixing the Zr and H_2BDC solutions when the H_2BDC/Zr ratio exceeded 3. Conversely, no precipitation occurred during spraying when the H_2BDC/Zr ratio was less than 2.5. The crystallinity of the sample increased with the H_2BDC/Zr ratio, and UiO-66 was formed when the H_2BDC/Zr ratio exceeded 2. Lower ratios result in reduced crystallinity. To achieve UiO-66 without preheating in spray synthesis, maintaining a BDC/Zr ratio in the range of 2–2.5 is crucial.

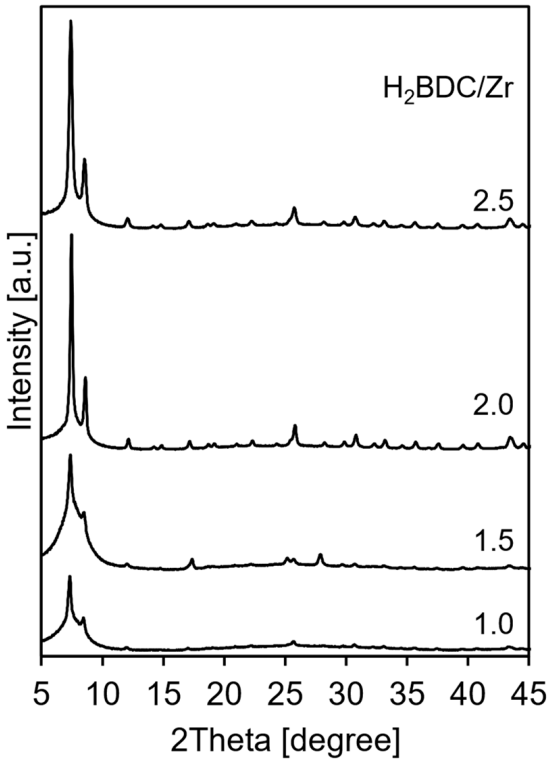

Figure 5. XRD patterns of spray-synthesized UiO-66 after washing with different H_2BDC/Zr ratios (AcOH/Zr = 440).

Because UiO-66 is crystallized by exchanging the acetate linker in the cluster with BDC^{2-} linkers, the deprotonation of H_2BDC to BDC^{2-} is required. The pH of the spray solution was 2.6 after mixing the Zr solution (AcOH/Zr = 440) and the H_2BDC solution (H_2BDC/Zr = 2.5). Considering the pKa values of 3.51 and 4.82 for H_2BDC, the existence rate of each dissociated species of H_2BDC in water is estimated to be <1% in BDC^{2-}, 10% in $HBDC^{-}$, and 90% as H_2BDC (Figure S9), although this is not an exact percentage because DMF is used as the solvent. Under highly acidic conditions, H_2BDC must exist at a ratio higher than the stoichiometric ratio (H_2BDC/Zr = 1).

Figure 6 shows the SEM images, nitrogen adsorption isotherms, and pore size distribution of the batch-synthesized UiO-66 and spray-synthesized UiO-66 before and after washing with $Zr(OnPr)_4$ as the Zr source at an AcOH/Zr ratio of 440 and H_2BDC/Zr ratio of 2.5. Hereafter, these three samples will be referred to as b-UiO-66(Pr), unwashed-sp-UiO-66(Pr), and sp-UiO-66(Pr).

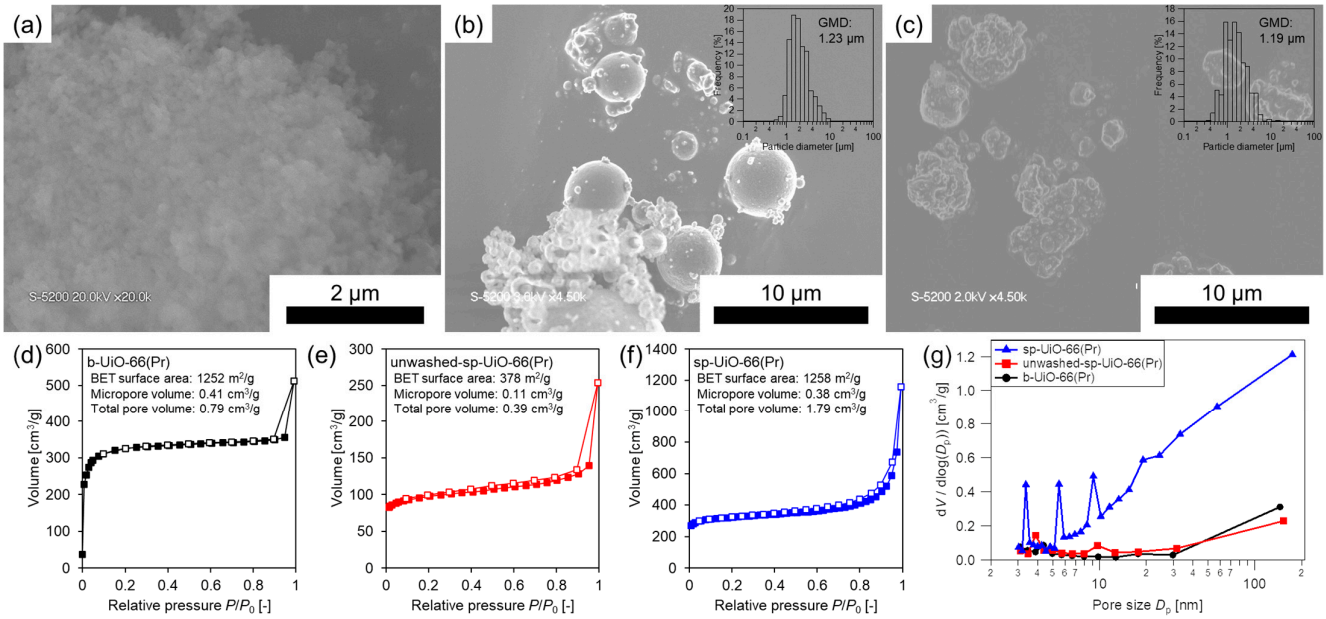

Figure 6. (**a**–**c**) SEM images, (**d**–**f**) nitrogen adsorption isotherms (filled: adsorption branch; opened: desorption branch), and (**g**) BJH pore size distribution of b-UiO-66(Pr), unwashed-sp-UiO-66(Pr), and sp-UiO-66(Pr); insets of (**b**,**c**) are particle size distributions.

In the SEM image of b-UiO-66 (Figure 6a), nanoparticles with diameters of approximately 150 nm are observed. The BET surface area and micropore volume of the sample are 1252 m^2/g and 0.41 cm^3/g, respectively, consistent with those for b-UiO-66(Cl).

Unwashed-sp-UiO-66(Pr) are spherical particles with a GMD of 1.23 μm (Figure 6b). However, for sp-UiO-66(Pr), the particles retain spherical morphology, but with a rough surface and GMD of 1.19 μm (Figure 6c). As described above, an excess amount of H_2BDC was required to obtain UiO-66 using $Zr(OnPr)_4$, which precipitated together with the UiO-66 crystals during droplet evaporation. The residual H_2BDC in unwashed-sp-UiO-66(Pr) was dissolved by a washing procedure, which resulted in the collapse of spherical particles, roughening the surface of sp-UiO-66(Pr). The BET surface areas are 378 m^2/g for the unwashed-sp-UiO-66(Pr) and 1258 m^2/g for sp-UiO-66(Pr). The low surface area of the unwashed-sp-UiO-66(Pr) was also due to clogging by residual H_2BDC. The total pore volume of sp-UiO-66(Pr) is 1.79 cm^3/g higher than that of b-UiO-66. The pore size distribution of sp-UiO-66(Pr) (Figure 6g) indicates that the sample has macropores that contribute to the high total pore volume, which is an interparticle void between the UiO-66 crystals produced by the dissolution of H_2BDC.

The TG-DTA curves (normalized to a final weight of 100%) of b-UiO-66(Pr) and sp-UiO-66(Pr) are shown in Figure 7. The TG curve of b-UiO-66(Pr) shows weight loss in the ranges of 25–100 °C, 150–270 °C, and 440–530 °C, where the DTA curve shows endothermic, small exothermic, and large exothermic peaks, respectively. The weight losses in these regions were due to the volatilization of physiosorbed solvents, dehydroxylation of the UiO-66 framework ($Zr_6(OH)_4O_4(BDC)_6 \rightarrow Zr_6O_6(BDC)_6 + 2H_2O$), and decomposition of BDC linkers [25,35,36]. By contrast, the TG-DTA curves of sp-UiO-66(Pr) show the weight loss of the decomposition of BDC linkers from 360 °C, indicating that the thermal stability was lower than that for b-UiO-66(Pr). The weight at 360 °C (W_{360}) and final weight (100%) were assigned to dehydrated UiO-66, $Zr_6O_{6+x}(BDC)_{6-x}$ (where x is the deficient value of BDC linkers per Zr_6 formula unit), and $6ZrO_2$, respectively. For ideal UiO-66, W_{360} is 220.2%. W_{360} and x were 217% and 0.16 for b-UiO-66(Pr), and 213% and 0.35 for sp-UiO-66(Pr), respectively, indicating that missing linker defects were present in both samples [8]. When AcOH was used as a modulator, a few acetate linkers remained in the UiO-66 crystals, resulting in the formation of missing linker defects [37]. In addition, sp-UiO-66(Pr) had more missing linker defects than that in b-UiO-66(Pr), because rapid UiO-66 crystallization during fast droplet evaporation did not complete the ligand exchange from acetate linkers to BDC linkers.

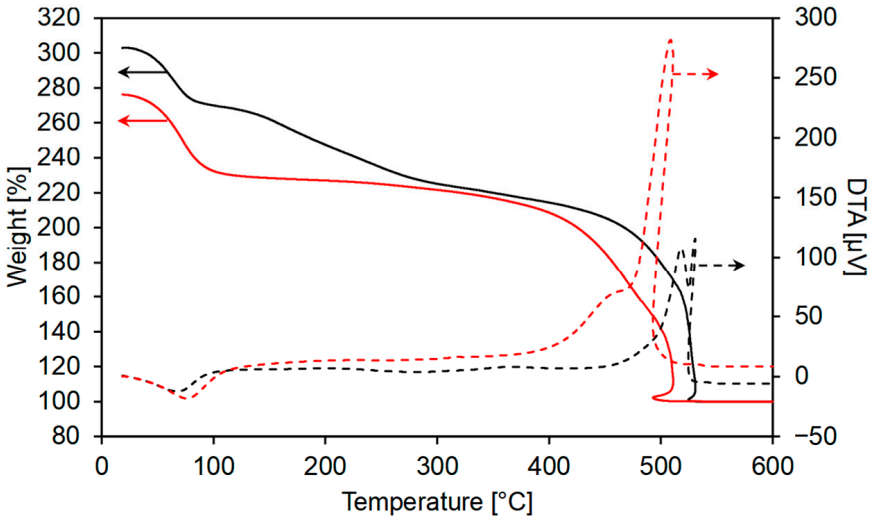

Figure 7. TG (solid line) and DTA (dashed line) curves of b-UiO-66(Pr) (black) and sp-UiO-66(Pr) (red).

Figure 8 shows the CO_2 adsorption isotherms at 273 and 298 K and the isosteric heat of adsorption (Q_{st}) for b-UiO-66(Pr) and sp-UiO-66(Pr). The CO_2 adsorption isotherms of sp-UiO-66(Pr) at 273 and 298 K were higher than those of b-UiO-66(Pr). CO_2 adsorption uptakes at 1 bar and 273 K are 2.87 mmol/g for b-UiO-66(Pr) and 3.43 mmol/g for sp-UiO-66(Pr), respectively. Q_{st} of sp-UiO-66(Pr) was higher than that of b-UiO-66(Pr). The high CO_2 uptake and Q_{st} values of sp-UiO-66(Pr) can be attributed to defects in the UiO-66 crystal skeleton generated by rapid crystallization. These defects act as CO_2 adsorption sites, resulting in a higher CO_2 uptake and Q_{st} [37,38].

Therefore, we successfully achieved the spray synthesis of UiO-66 without preheating using $Zr(OnPr)_4$ and acetic acid for cluster formation at room temperature with a short aging time. The yield and purity for sp-UiO-66(Pr) were 1.1 mg/mL and 65%, respectively. When 15 mL of the precursor solution was used, the yield per time was 7.3 mg/h higher than that for b-UiO-66(Pr) (1.9 mg/h). Based on this knowledge, the amino functional group-substituted UiO-66 (UiO-66-NH_2) was also spray synthesized and analyzed in detail alongside spray-synthesized UiO-66.

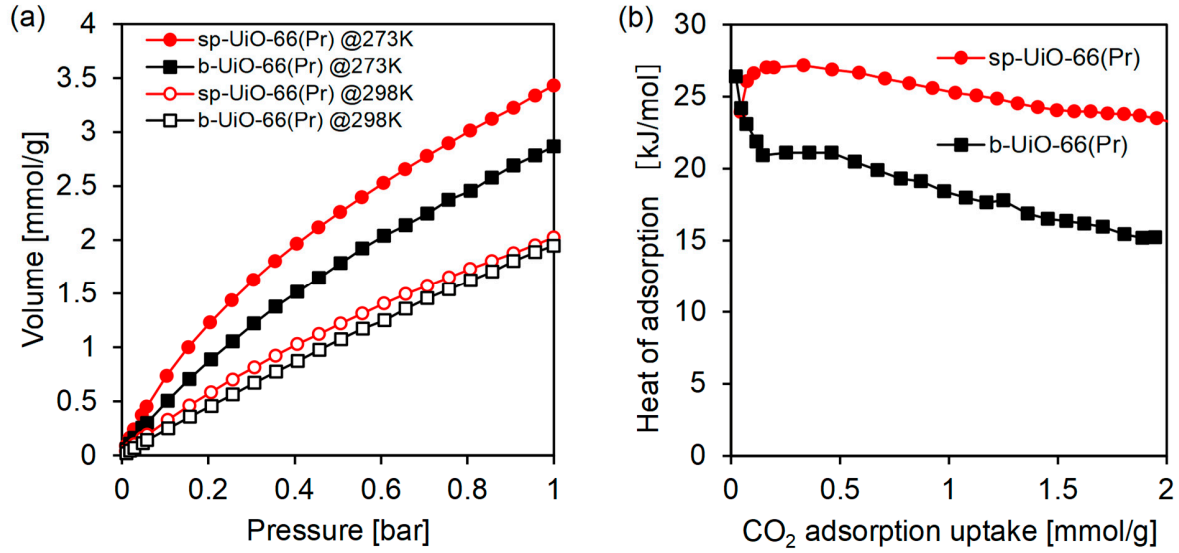

Figure 8. (**a**) CO_2 adsorption isotherms at 273 K and 298 K and (**b**) isosteric heat of adsorption of the b-UiO-66(Pr) and sp-UiO-66(Pr).

3.3. Spray Synthesis of UiO-66-NH_2 Using Zr(OnPr)$_4$ as a Zr Source without Preheating

UiO-66-NH_2 was spray synthesized using 2-aminoterephthalic acid (H_2BDC-NH_2) instead of H_2BDC after the formation of Zr acetate clusters. Figure S10 shows the XRD patterns of spray synthesizing with varying H_2BDC-NH_2/Zr ratios in the range of 2.5–6.0. However, low crystalline UiO-66-NH_2 was obtained at the ratio of 4.0–5.0, despite partial deprotonation of the carboxylic groups of H_2BDC-NH_2 owing to the lower pKa values of 3.6 and 3.1 compared to those of H_2BDC.

Schaate et al. reported that the synthesis of H_2O is essential for obtaining crystalline UiO-66-NH_2 [20]. Therefore, water was added to the Zr solution at a H_2O/Zr ratio of 1. The XRD pattern of the spray-synthesized UiO-66-NH_2 with the addition of H_2O exhibited UiO-66 crystal patterns consistent with those of batch-synthesized UiO-66-NH_2 (Figure 9). However, the addition of H_2O to the H_2BDC-NH_2 solution did not yield crystalline UiO-66-NH_2. This indicates that the addition of H_2O to the Zr solution assisted in the formation of Zr-acetate clusters, resulting in highly crystalline UiO-66-NH_2.

Figure 10 shows the SEM images, nitrogen adsorption isotherms, and pore size distribution of batch-synthesized UiO-66-NH_2 and spray-synthesized UiO-66-NH_2 before and after washing with Zr(O*n*Pr)$_4$ as the Zr source at an AcOH/Zr ratio of 440 and H_2BDC-NH_2/Zr ratio of 5. Hereafter, the three samples are referred to as b-UiO-66-NH_2(Pr), unwashed-sp-UiO-66-NH_2(Pr), and sp-UiO-66-NH_2(Pr).

The SEM image of b-UiO-66-NH_2(Pr) (Figure 10a) shows nanoparticles with diameters of approximately 200 nm. The BET surface area and micropore volume of the sample are 1319 m^2/g and 0.42 cm^3/g, respectively, slightly higher than those of b-UiO-66(Cl) and b-UiO-66(Pr).

The morphologies of the unwashed-sp-UiO-66-NH_2(Pr) and sp-UiO-66-NH_2(Pr) (Figure 10b,c) were similar to those of the unwashed-sp-UiO-66(Pr) and sp-UiO-66(Pr). Unwashed-sp-UiO-66-NH_2(Pr) are spherical particles with a GMD of 1.32 μm, whereas sp-UiO-66-NH_2(Pr) are partially collapsed spherical particles with rough surface and a GMD of 1.26 μm. The rough surface of sp-UiO-66-NH_2(Pr) was due to the dissolution of the residual H_2BDC-NH_2, similar to that of sp-UiO-66(Pr). The BET surface area of unwashed-sp-UiO-66(Pr) is significantly low at 59 m^2/g due to the residual H_2BDC-NH_2. By contrast, the BET surface area and total pore volume of sp-UiO-66-NH_2(Pr) were 1263 m^2/g and 2.33 cm^3/g, respectively. These high values were due to the dissolution of the residual H_2BDC-NH_2 which opened the micropores of the UiO-66-NH_2 crystals and produced macropores, as confirmed by the pore size distribution (Figure 10g).

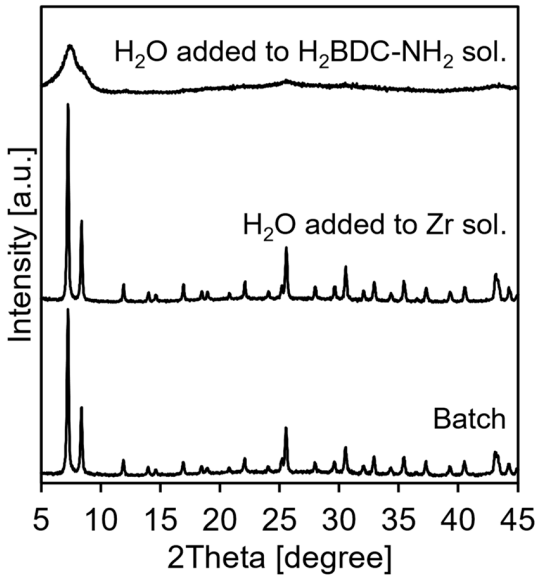

Figure 9. XRD patterns of batch-synthesized and spray-synthesized UiO-66-NH_2 with the addition of H_2O to Zr and H_2BDC-NH_2 solutions (total molar ratio is $Zr(O_nPr)_4$:H_2BDC-NH_2:DMF:AcOH:H_2O = 1:5:754:440:1).

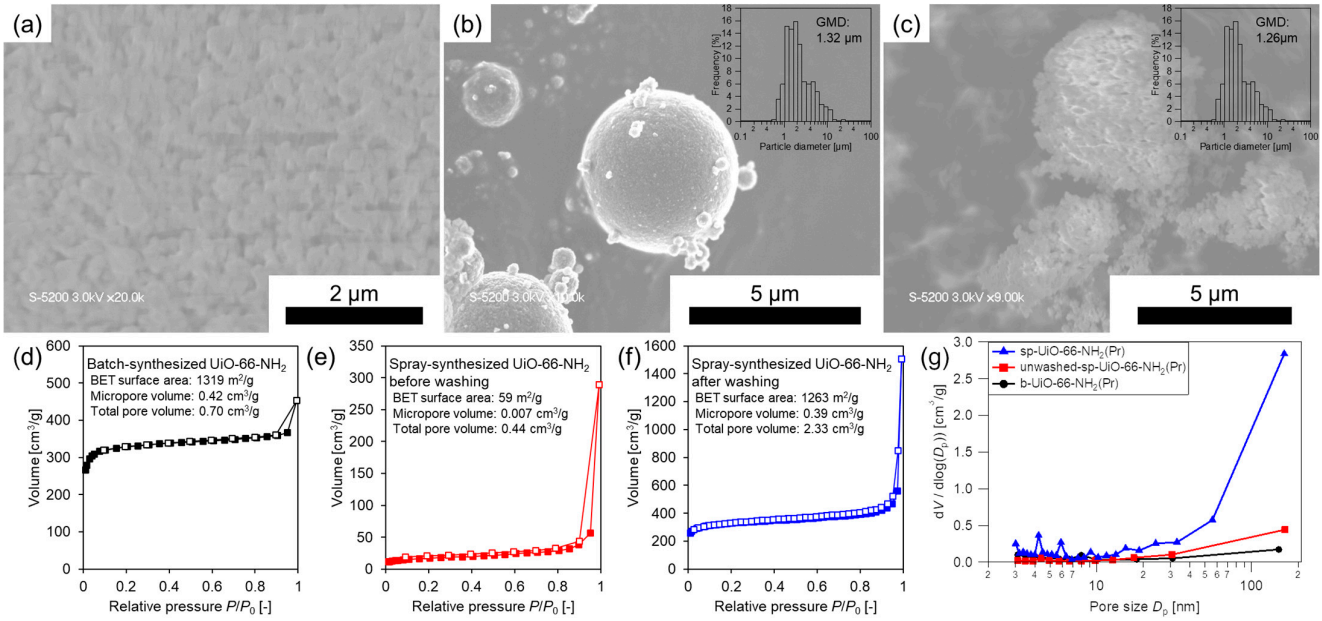

Figure 10. (**a**–**c**) SEM images, (**d**–**f**) nitrogen adsorption isotherms (filled: adsorption branch; opened: desorption branch), and (**g**) BJH pore size distribution of UiO-66-NH_2 using $Zr(OnPr)_4$ as the Zr source: (**a**,**d**) batch-synthesized UiO-66 is spray-synthesized (**b**,**e**) before and (**c**,**f**) after washing. Insets of (**b**,**c**) are particle size distributions.

The yield and purity for sp-UiO-66-NH_2(Pr) were 1.4 mg/mL and 69%, respectively. When 15 mL of the precursor solution was used, the yield per time was 9.0 mg/h higher than that for b-UiO-66-NH_2(Pr) (2.1 mg/h).

The TG-DTA curves (normalized to a final weight of 100%) of b-UiO-66-NH_2(Pr) and sp-UiO-66-NH_2(Pr) are shown in Figure 11. Both samples exhibited similar weight losses in the TG curves. From the DTA curves, the decomposition of BDC-NH_2 linkers starts from 300 °C. Thus, the weight losses in the ranges of 25–100 °C, 150–300 °C, and 300–450 °C are due to the volatilization of physiosorbed solvents, dehydroxylation of UiO-66-NH_2

framework ($Zr_6(OH)_4O_4(BDC\text{-}NH_2)_6 \rightarrow Zr_6O_6(BDC\text{-}NH_2)_6 + 2H_2O$), and decomposition of BDC-NH_2 linkers, respectively. This implies that sp-UiO-66-NH_2(Pr) had a consistent thermal stability with b-UiO-66-NH_2(Pr). Similar to the case of UiO-66, the weights at 300 °C (W_{300}) are assigned to dehydrated UiO-66-NH_2 ($Zr_6O_{6+y}(BDC\text{-}NH_2)_{6-y}$) and 6$ZrO_2$, respectively. For ideal UiO-66-NH_2, W_{300} was 232.4%. The W_{300} and y are 217% and 0.63 for b-UiO-66-NH_2(Pr), and 213% and 0.84 for sp-UiO-66-NH_2(Pr), respectively. Similar to UiO-66, sp-UiO-66-NH_2(Pr) had more missing linker defects than b-UiO-66(Pr) because of rapid UiO-66-NH_2 crystallization during droplet evaporation.

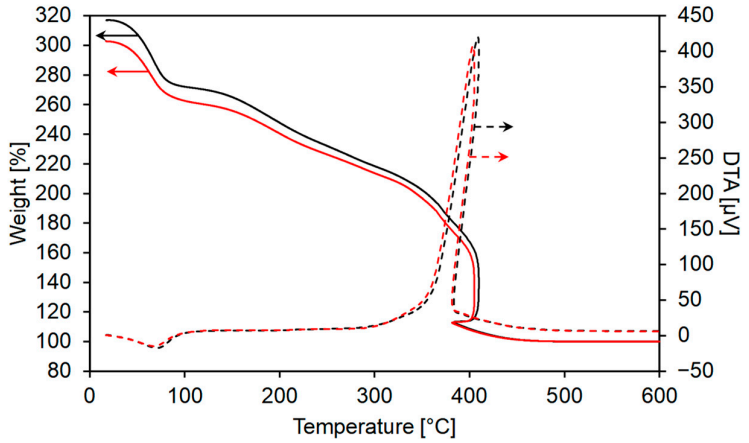

Figure 11. TG (solid line) and DTA (dashed line) curves of b-UiO-66-NH_2(Pr) (black) and sp-UiO-66-NH_2(Pr) (red).

Figure 12 shows the CO_2 adsorption isotherms at 273 and 298 K and Q_{st} of b-UiO-66-NH_2(Pr) and sp-UiO-66-NH_2(Pr). The CO_2 adsorption uptake of sp-UiO-66-NH_2(Pr) at 273 and 298 K was higher than that of b-UiO-66-NH_2(Pr). CO_2 adsorption uptakes at 1 bar and 273 K are 4.81 mmol/g for b-UiO-66(Pr) and 6.11 mmol/g for sp-UiO-66(Pr). These values are higher than those of b-UiO-66(Pr) and sp-UiO-66(Pr) because the NH_2 functional group has a high affinity for CO_2 molecules [39]. Q_{st} of sp-UiO-66-NH_2(Pr) was higher than that of b-UiO-66-NH_2(Pr). The high CO_2 uptake and Q_{st} values of sp-UiO-66-NH_2(Pr) can be attributed to defects in the UiO-66-NH_2 crystal skeleton generated by rapid crystallization.

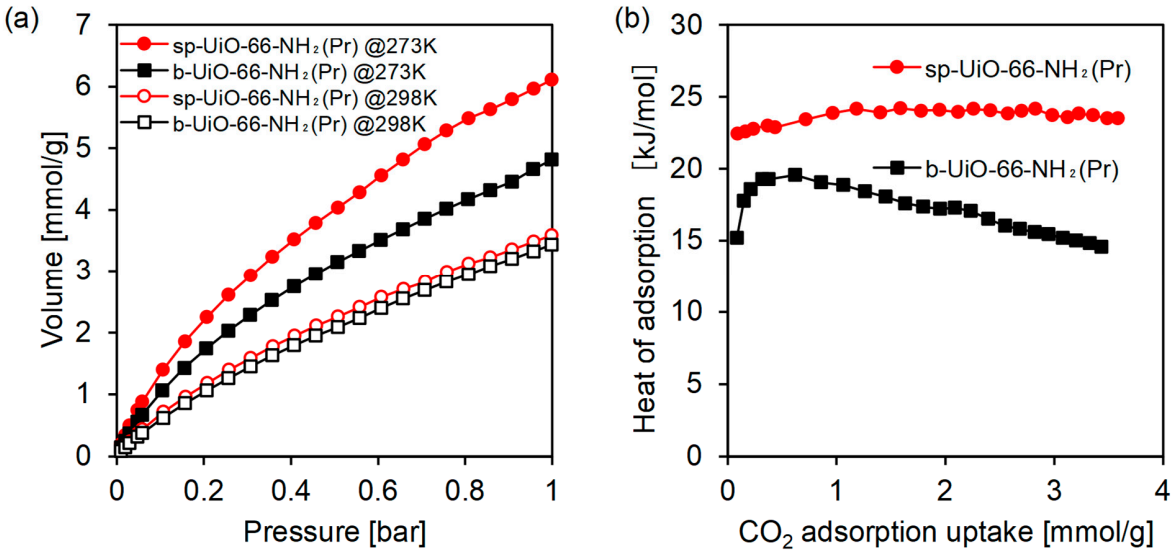

Figure 12. (**a**) CO_2 adsorption isotherms at 273 K and 298 K and (**b**) isosteric heat of adsorption of the b-UiO-66-NH_2(Pr) and sp-UiO-66-NH_2(Pr).

4. Conclusions

In conclusion, we successfully demonstrated the spray synthesis of UiO-66 and UiO-66-NH_2 without preheating using $Zr(OnPr)_4$ as the Zr source and acetic acid for cluster formation. This approach eliminates the need for additional preheating steps that are required when using $ZrCl_4$ as the Zr source. The spray-synthesized UiO-66 and UiO-66-NH_2 exhibited spherical morphologies with interparticle voids that contributed to high total pore volumes without compromising the BET surface areas and micropore volumes. Furthermore, we investigated the CO_2 adsorption capacities of the spray-synthesized MOFs. UiO-66 and UiO-66-NH_2 exhibited a higher CO_2 adsorption uptake and Q_{st} than the batch-synthesized sample, which was attributed to missing linker defects in the crystal structure introduced by rapid droplet evaporation. This study contributes to the understanding of the spray synthesis process and provides insight into the mechanisms governing the formation of MOFs in droplets. These findings will pave the way for further advancements in the controlled synthesis of UiO-66 and related MOFs, thereby expanding their applicability in various fields, including gas adsorption and catalysis.

Supplementary Materials: The supporting information can be downloaded at: https://www.mdpi.com/article/10.3390/cryst14020116/s1, Figure S1: Schematic of the homemade apparatus; Figure S2, S3, S6–S8 and S10: XRD patterns; Figure S4: Nitrogen adsorption-desorption isotherms; Figure S5: Estimated dimensionless diameter of droplets as a function of evaporation time with initial diameters of 10 μm at different temperature; Figure S9: Estimated existence rate of each dissociated species of H_2BDC in water.

Author Contributions: Conceptualization, writing—original draft preparation, visualization, supervision, and project administration, M.K.; methodology, validation, and investigation, M.K., Y.M. and Y.U.; resources, M.K. and M.S.; data curation, M.K. and Y.M.; writing—review and editing, M.K., Y.M., Y.U. and M.S.; funding acquisition, M.K. and M.S. All authors have read and agreed to the published version of the manuscript.

Funding: This study was supported in part by a Grant-in-Aid for Young Scientists (A) no. 16H06128 and Grant-in-Aid for Scientific Research (C) nos. 20K05209 and 21K04750 of the Japan Society for the Promotion of Science.

Data Availability Statement: Data are contained within the article.

Conflicts of Interest: The authors declare no conflicts of interest.

References

1. Bradshaw, D.; Garai, A.; Huo, J. Metal-Organic Framework Growth at Functional Interfaces: Thin Films and Composites for Diverse Applications. *Chem. Soc. Rev.* **2012**, *41*, 2344–2381. [CrossRef] [PubMed]
2. Falcaro, P.; Ricco, R.; Yazdi, A.; Imaz, I.; Furukawa, S.; Maspoch, D.; Ameloot, R.; Evans, J.D.; Doonan, C.J. Application of Metal and Metal Oxide Nanoparticles@MOFs. *Coord. Chem. Rev.* **2016**, *307*, 237–254. [CrossRef]
3. Yuan, S.; Feng, L.; Wang, K.; Pang, J.; Bosch, M.; Lollar, C.; Sun, Y.; Qin, J.; Yang, X.; Zhang, P.; et al. Stable Metal-Organic Frameworks: Design, Synthesis, and Applications. *Adv. Mater.* **2018**, *30*, e1704303. [CrossRef] [PubMed]
4. Chen, Z.; Kirlikovali, K.O.; Li, P.; Farha, O.K. Reticular Chemistry for Highly Porous Metal-Organic Frameworks: The Chemistry and Applications. *Acc. Chem. Res.* **2022**, *55*, 579–591. [CrossRef]
5. Rabiee, N.; Atarod, M.; Tavakolizadeh, M.; Asgari, S.; Rezaei, M.; Akhavan, O.; Pourjavadi, A.; Jouyandeh, M.; Lima, E.C.; Hamed Mashhadzadeh, A.; et al. Green Metal-Organic Frameworks (MOFs) for Biomedical Applications. *Microporous Mesoporous Mater.* **2022**, *335*, 111670. [CrossRef]
6. Bai, Y.; Dou, Y.; Xie, L.-H.; Rutledge, W.; Li, J.-R.; Zhou, H.-C. Zr-Based Metal-Organic Frameworks: Design, Synthesis, Structure, and Applications. *Chem. Soc. Rev.* **2016**, *45*, 2327–2367. [CrossRef]
7. Cavka, J.H.; Jakobsen, S.; Olsbye, U.; Guillou, N.; Lamberti, C.; Bordiga, S.; Lillerud, K.P. A New Zirconium Inorganic Building Brick Forming Metal Organic Frameworks with Exceptional Stability. *J. Am. Chem. Soc.* **2008**, *130*, 13850–13851. [CrossRef] [PubMed]
8. Winarta, J.; Shan, B.; Mcintyre, S.M.; Ye, L.; Wang, C.; Liu, J.; Mu, B. A Decade of UiO-66 Research: A Historic Review of Dynamic Structure, Synthesis Mechanisms, and Characterization Techniques of an Archetypal Metal–Organic Framework. *Cryst. Growth Des.* **2020**, *20*, 1347–1362. [CrossRef]
9. Julien, P.A.; Mottillo, C.; Friščić, T. Metal–Organic Frameworks Meet Scalable and Sustainable Synthesis. *Green Chem.* **2017**, *19*, 2729–2747. [CrossRef]

10. Rubio-Martinez, M.; Avci-Camur, C.; Thornton, A.W.; Imaz, I.; Maspoch, D.; Hill, M.R. New Synthetic Routes towards MOF Production at Scale. *Chem. Soc. Rev.* **2017**, *46*, 3453–3480. [CrossRef]
11. Ameloot, R.; Vermoortele, F.; Vanhove, W.; Roeffaers, M.B.J.; Sels, B.F.; De Vos, D.E. Interfacial Synthesis of Hollow Metal-Organic Framework Capsules Demonstrating Selective Permeability. *Nat. Chem.* **2011**, *3*, 382–387. [CrossRef] [PubMed]
12. Gimeno-Fabra, M.; Munn, A.S.; Stevens, L.A.; Drage, T.C.; Grant, D.M.; Kashtiban, R.J.; Sloan, J.; Lester, E.; Walton, R.I. Instant MOFs: Continuous Synthesis of Metal-Organic Frameworks by Rapid Solvent Mixing. *Chem. Commun.* **2012**, *48*, 10642–10644. [CrossRef]
13. He, B.; Sadiq, M.M.; Batten, M.P.; Suzuki, K.; Rubio-Martinez, M.; Gardiner, J.; Hill, M.R. Continuous Flow Synthesis of a Zr Magnetic Framework Composite for Post-Combustion CO_2 Capture. *Chemistry* **2019**, *25*, 13184–13188. [CrossRef] [PubMed]
14. Rubio-Martinez, M.; Batten, M.P.; Polyzos, A.; Carey, K.-C.; Mardel, J.I.; Lim, K.-S.; Hill, M.R. Versatile, High Quality and Scalable Continuous Flow Production of Metal-Organic Frameworks. *Sci. Rep.* **2014**, *4*, 5443. [CrossRef]
15. McKinstry, C.; Cathcart, R.J.; Cussen, E.J.; Fletcher, A.J.; Patwardhan, S.V.; Sefcik, J. Scalable Continuous Solvothermal Synthesis of Metal Organic Framework (MOF-5) Crystals. *Chem. Eng. J.* **2016**, *285*, 718–725. [CrossRef]
16. Carné-Sánchez, A.; Imaz, I.; Cano-Sarabia, M.; Maspoch, D. A Spray-Drying Strategy for Synthesis of Nanoscale Metal-Organic Frameworks and Their Assembly into Hollow Superstructures. *Nat. Chem.* **2013**, *5*, 203–211. [CrossRef] [PubMed]
17. Garzón-Tovar, L.; Cano-Sarabia, M.; Carné-Sánchez, A.; Carbonell, C.; Imaz, I.; Maspoch, D. A Spray-Drying Continuous-Flow Method for Simultaneous Synthesis and Shaping of Microspherical High Nuclearity MOF Beads. *React. Chem. Eng.* **2016**, *1*, 533–539. [CrossRef]
18. Kubo, M.; Saito, T.; Shimada, M. Evaluation of the Parameters Utilized for the Aerosol-Assisted Synthesis of HKUST-1. *Microporous Mesoporous Mater.* **2017**, *245*, 126–132. [CrossRef]
19. Kubo, M.; Kitano, T.; Shimada, M. Spray Synthesis of Hierarchical Porous Metal-Organic Framework HKUST-1 with Soft Templates and Methylene Blue Adsorption Performance. *Adv. Powder Technol.* **2024**, *35*, 104280. [CrossRef]
20. Schaate, A.; Roy, P.; Godt, A.; Lippke, J.; Waltz, F.; Wiebcke, M.; Behrens, P. Modulated Synthesis of Zr-Based Metal-Organic Frameworks: From Nano to Single Crystals. *Chemistry* **2011**, *17*, 6643–6651. [CrossRef]
21. Kubo, M.; Ishimura, M.; Shimada, M. Improvement of Production Efficiency of Spray-Synthesized HKUST-1. *Adv. Powder Technol.* **2021**, *32*, 2370–2378. [CrossRef]
22. Kubo, M.; Matsumoto, T.; Shimada, M. Spray Synthesis of Pd Nanoparticle Incorporated HKUST-1, and Its Catalytic Activity for 4-Nitrophenol Reduction. *Adv. Powder Technol.* **2022**, *33*, 103701. [CrossRef]
23. Chen, X.; Li, Y.; Fu, Q.; Qin, H.; Lv, J.; Yang, K.; Zhang, Q.; Zhang, H.; Wang, M. An Efficient Modulated Synthesis of Zirconium Metal-Organic Framework UiO-66. *RSC Adv.* **2022**, *12*, 6083–6092. [CrossRef] [PubMed]
24. Okuyama, K.; Abdullah, M.; Wuled Lenggoro, I.; Iskandar, F. Preparation of Functional Nanostructured Particles by Spray Drying. *Adv. Powder Technol.* **2006**, *17*, 587–611. [CrossRef]
25. Zhao, Y.; Zhang, Q.; Li, Y.; Zhang, R.; Lu, G. Large-Scale Synthesis of Monodisperse UiO-66 Crystals with Tunable Sizes and Missing Linker Defects via Acid/Base Co-Modulation. *ACS Appl. Mater. Interfaces* **2017**, *9*, 15079–15085. [CrossRef]
26. Schoenecker, P.M.; Belancik, G.A.; Grabicka, B.E.; Walton, K.S. Kinetics Study and Crystallization Process Design for Scale-up of UiO-66-NH_2 synthesis. *AIChE J.* **2013**, *59*, 1255–1262. [CrossRef]
27. Xu, H.; Sommer, S.; Broge, N.L.N.; Gao, J.; Iversen, B.B. The Chemistry of Nucleation: In Situ Pair Distribution Function Analysis of Secondary Building Units During UiO-66 MOF Formation. *Chemistry* **2019**, *25*, 2051–2058. [CrossRef]
28. Butova, V.V.; Budnyk, A.P.; Charykov, K.M.; Vetlitsyna-Novikova, K.S.; Lamberti, C.; Soldatov, A.V. Water as a Structure-Driving Agent between the UiO-66 and MIL-140A Metal-Organic Frameworks. *Chem. Commun.* **2019**, *55*, 901–904. [CrossRef]
29. Ordoubadi, M.; Gregson, F.K.A.; Melhem, O.; Barona, D.; Miles, R.E.H.; D'Sa, D.; Gracin, S.; Lechuga-Ballesteros, D.; Reid, J.P.; Finlay, W.H.; et al. Multi-Solvent Microdroplet Evaporation: Modeling and Measurement of Spray-Drying Kinetics with Inhalable Pharmaceutics. *Pharm. Res.* **2019**, *36*, 100. [CrossRef]
30. Katz, M.J.; Brown, Z.J.; Colón, Y.J.; Siu, P.W.; Scheidt, K.A.; Snurr, R.Q.; Hupp, J.T.; Farha, O.K. A Facile Synthesis of UiO-66, UiO-67 and Their Derivatives. *Chem. Commun.* **2013**, *49*, 9449–9451. [CrossRef]
31. Tulig, K.; Walton, K.S. An Alternative UiO-66 Synthesis for HCl-Sensitive Nanoparticle Encapsulation. *RSC Adv.* **2014**, *4*, 51080–51083. [CrossRef]
32. DeStefano, M.R.; Islamoglu, T.; Garibay, S.J.; Hupp, J.T.; Farha, O.K. Room-Temperature Synthesis of UiO-66 and Thermal Modulation of Densities of Defect Sites. *Chem. Mater.* **2017**, *29*, 1357–1361. [CrossRef]
33. Puchberger, M.; Kogler, F.R.; Jupa, M.; Gross, S.; Fric, H.; Kickelbick, G.; Schubert, U. Can the Clusters $Zr_6O_4(OH)_4(OOCR)_{12}$ and $[Zr_6O_4(OH)_4(OOCR)_{12}]_2$ Be Converted into Each Other? *Eur. J. Inorg. Chem.* **2006**, *2006*, 3283–3293. [CrossRef]
34. Karadeniz, B.; Howarth, A.J.; Stolar, T.; Islamoglu, T.; Dejanović, I.; Tireli, M.; Wasson, M.C.; Moon, S.-Y.; Farha, O.K.; Friščić, T.; et al. Benign by Design: Green and Scalable Synthesis of Zirconium UiO-Metal–Organic Frameworks by Water-Assisted Mechanochemistry. *ACS Sustain. Chem. Eng.* **2018**, *6*, 15841–15849. [CrossRef]
35. Valenzano, L.; Civalleri, B.; Chavan, S.; Bordiga, S.; Nilsen, M.H.; Jakobsen, S.; Lillerud, K.P.; Lamberti, C. Disclosing the Complex Structure of UiO-66 Metal Organic Framework: A Synergic Combination of Experiment and Theory. *Chem. Mater.* **2011**, *23*, 1700–1718. [CrossRef]
36. Shearer, G.C.; Chavan, S.; Ethiraj, J.; Vitillo, J.G.; Svelle, S.; Olsbye, U.; Lamberti, C.; Bordiga, S.; Lillerud, K.P. Tuned to Perfection: Ironing out the Defects in Metal–Organic Framework UiO-66. *Chem. Mater.* **2014**, *26*, 4068–4071. [CrossRef]

37. Wu, H.; Chua, Y.S.; Krungleviciute, V.; Tyagi, M.; Chen, P.; Yildirim, T.; Zhou, W. Unusual and Highly Tunable Missing-Linker Defects in Zirconium Metal-Organic Framework UiO-66 and Their Important Effects on Gas Adsorption. *J. Am. Chem. Soc.* **2013**, *135*, 10525–10532. [CrossRef]
38. Zhou, C.; Li, H.; Qin, H.; Yuan, B.; Zhang, M.; Wang, L.; Yang, B.; Tao, C.-A.; Zhang, S. Defective UiO-66-NH2 Monoliths for Optimizing CO_2 Capture Performance. *Chem. Eng. J.* **2023**, *467*, 143394. [CrossRef]
39. Ethiraj, J.; Albanese, E.; Civalleri, B.; Vitillo, J.G.; Bonino, F.; Chavan, S.; Shearer, G.C.; Lillerud, K.P.; Bordiga, S. Carbon Dioxide Adsorption in Amine-functionalized Mixed-ligand Metal–Organic Frameworks of UiO-66 Topology. *ChemSusChem* **2014**, *7*, 3382–3388. [CrossRef]

Disclaimer/Publisher's Note: The statements, opinions and data contained in all publications are solely those of the individual author(s) and contributor(s) and not of MDPI and/or the editor(s). MDPI and/or the editor(s) disclaim responsibility for any injury to people or property resulting from any ideas, methods, instructions or products referred to in the content.